International
Solar Energy Society

EXPERIMENTAL INVESTIGATIONS OF HEAT EXCHANGERS IN ICE STORAGES FOR COMBINED SOLAR AND HEAT PUMP SYSTEMS.

Daniel Carbonell , Martin Granzotto, Mattia Battaglia, Daniel Philippen and Michel Y. Haller.

SPF, Institut für Solartechnik , HSR, Hochschule für Technik ,
CH-8640 Rapperswil, Switzerland

Abstract

In the present paper different heat exchangers designed to be installed into an ice storage for solar and heat pump heating applications are experimentally investigated. Analyzed heat exchangers are capillary mats and flat plate types. For each heat exchanger, different designs, materials and number of heat exchanger units are evaluated using two different mass flows. This paper aims at i) characterizing different heat exchanger designs by means of measurements in a laboratory-size ice storage of 2 m^3, ii) determine specific advantages and disadvantages of different heat exchanger concepts for ice storages used in combination with solar collectors and a heat pump and iii) provide a source of experimental data for model validation.

Keywords: ice storage, heat exchangers, solar-ice.

Nomenclature

A_{ext}	external area of one hx [m^2]	Q	energy delivered to the storage [kWh]
A_{hx}	total hx area in the storage [m^2]	$T_{w,avg}$	averaged storage temperature [^{o}C]
d_i	inside diameter of CM tubes [m]	$T_{f,in}$	heat transfer fluid temperature at the inlet of the hx [^{o}C]
d_o	outside diameter of CM tubes [m]	$T_{f,out}$	heat transfer fluid temperature at the outlet of the hx [^{o}C]
H_{hx}	height of FP hx [m]	U	heat transfer coefficient of the hx [W/(m^{2}K)]
L_{tube}	length of U-shape tubes [m]	$\dot{V}_n$	nominal volume flow of the experiments [l/h]
L_{hx}	length of FP hx [m]	V_r	ice fraction [kg$_{ice}$/kg$_{water}$]
$\dot{m}$	mass flow rate of the brine [kg/s]	V_r^*	ice fraction calculated from energy exchanged [kg_{ice}/kg_{water}]
n_{hx}	number of hx in the storage	x_{tubes}	distance between tubes in one CM [mm]
n_{tubes}	number of tubes in one CM	x_{hx}	distance between hxs [mm]
CM	capillar mats	Nu	Nusselt number
FP	flat plate	PP	polypropylene
G-type	commercial name of a CM	Re	Reynolds number
heating	energy provided to the storage	SS	stainless steel
hx	heat exchanger	S-type	commercial name of a CM

1. Introduction

Ice storages are a well proven technology for cooling applications where their main role consists in peak shaving of cooling loads at noon or in providing high cooling power for industrial processes (ASHRAE, 2007). On the other hand, ice storages can also be used for solar heating applications where less extraction power is needed because they serve as heat source for a heat pump and not to cover peak demands. Therefore, ice storages used in solar heating applications, in so-called solar-ice systems, can be designed with less heat exchanger area per storage unit volume compared to cooling applications (Carbonell et al., 2016b). However, this is not often the case when companies that have been traditionally working for the cooling sector are trying to enter the solar heating market designing the ice storage with the experience gained from cooling applications only.

In solar-ice applications, it is important to provide ice storages at low cost in order to be competitive with respect to alternative solutions such as boreholes for ground source heat pump systems. Furthermore, ice storages have to be reliable to keep maintenance costs as low as possible. In order to reduce installation costs, a de-icing concept can be used to avoid installing heat exchangers in the whole ice storage volume (Philippen et al. (2012),Carbonell et al. (2015)). However, for small ice storages, e.g. below 10 m^3, the ice fraction that can be achieved using a de-icing concept is significantly smaller than using a non de-icing concept. For single family houses, a solar-ice system with a large ice storage, e.g. higher than 10 m^3, will most likely not be cost competitive compared to a ground source heat pump system. Therefore, for single-family houses, ice storages based on a non de-icing concept seem to be a more attractive solution. Moreover, market available ice storages are based on a non de-icing concept, not only for small, but also for large ice storages. Most of ice storages installed in Europe are based on ice-on-coil heat exchangers, and although other heat exchanger concepts exist on the market, their specific advantages and disadvantages remain unclear.

This paper is focused on the experimental analyses of several heat exchangers for ice storage concepts that do not use a de-icing concept. The aim is to compare different heat exchanger concepts in terms of efficiency and cost with the final goal to define the cost effective heat exchanger area needed for solar heating applications. In order to achieve the final goal, it is necessary to simulate the complete solar-ice system with a well validated ice storage model that is able to consider all heat exchanger designs. Therefore, the experimental data presented in this paper will be used to validate an ice storage model in a second step. Examples of complete solar-ice system simulations can be found in recent publications, e.g. Trinkl et al. (2009), Tamasauskas et al. (2012), Winteler et al. (2014) and Carbonell et al. (2016a). Moreover, the experiments presented in the paper are also helpful to understand the physics behind the solidification and melting of ice on the different heat exchangers.

2. Experiments

2.1. Experimental set-up

The scheme of the experimental set-up is shown in Fig. 1. The inner dimensions of the ice storage are 2 m x 1 m x 1.3 m and it is insulated with 5 cm of Armaflex® ($\lambda = 0.041\ W/(m \cdot K)$). The storage is filled with 2 m^3 of water. The heating and cooling is provided by a chiller with approximately 6 kW heating and cooling power. Five Pt100 sensors are installed inside the storage for measuring the temperature at different heights. Three Pt100 sensors are installed at the inlet/outlet of the heat exchangers, considering two possibilities for loading/unloading. An ultrasonic sensor is used to measure the height of the water level and to derive the total fraction of ice inside the storage. A volume flow sensor is installed and the volume flow is regulated by a PID control. A LabVIEW interface has been developed to run all testing sequences automatically.
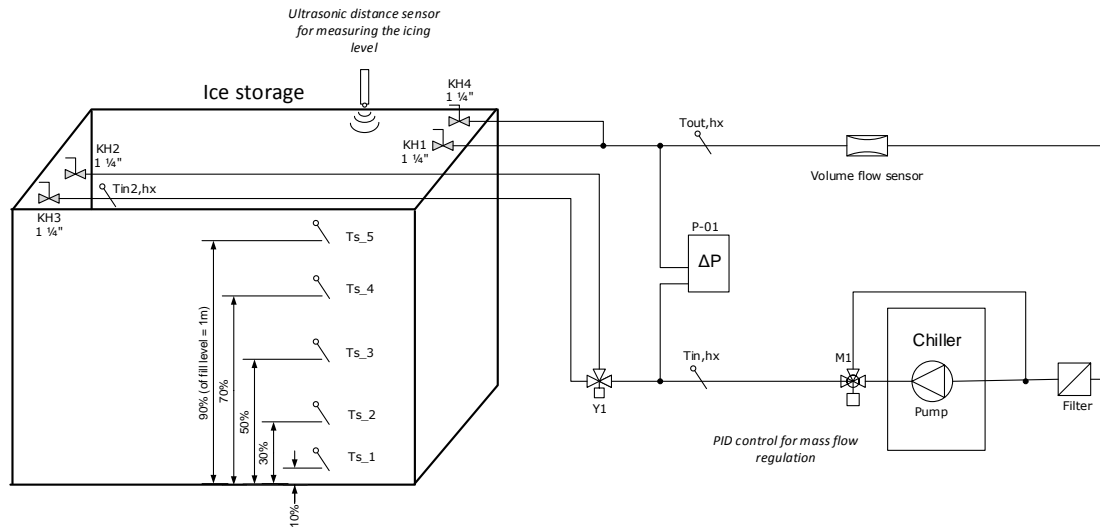
Fig. 1: Hydraulic scheme of the experimental set-up with sensor locations.

2.2. Measurement uncertainties

The temperature sensors have been calibrated in a Fluke Dry-Block Calibrator for the temperature range of the test cycles ($(-10) - 40°C$). Based on the calibration, the output values of each temperature sensor were corrected according to a 1st order polynomial. The remaining uncertainty of the Pt100 sensors after calibration was in the order of 0.03-0.04 K. The mass flow rate measurement was done using a magnetic flow meter, that has been calibrated for flows between 500 and 1400 l/h. The relative uncertainty of the volume flow rate measurement after the calibration of the flow sensor was determined to be 0.6% . For the glycol concentration, an acceptable range of 31.92%-34.66% has been defined. The maximal relative uncertainty of the mixture density is then estimated to be 1.0%. The relative uncertainty of the specific heat capacity is smaller than 1.3%. All these uncertainty values are used to calculate the total uncertainty of the derived values such as power or heat transfer coefficient. The relative uncertainty of the extracted power is in the order of 2%. The calculated heat transfer coefficient is affected by an uncertainty that ranges from 2.5% up to 14%. High uncertainty values are caused by small temperature differences when the ice storage temperature approaches the chiller set point temperature. Thus, system operating points with significant energy transfer are not affected by this large uncertainty values. The ice fraction calculation was done based on the changing water level in the storage tank when ice is formed or melted. The ultrasonic sensor has a precision of 0.5 mm which results in an uncertainty of the icing fraction in the order of 0.5%-1%.

2.3. Heat exchangers tested

Two capillary mats (CM) from the manufacturer Clina have been experimentally evaluated: G and S-type. All CM are made with the same kind of tubes and materials but have a slightly different design (see Fig. 2). In the S-type, the U-shape of the tube observed in the G-type is modified and the down-flow and up-flow on each tube are on the same plane. Therefore, S-types are plane and G-types are U-shaped. The G-type has 22% more heat exchanger area than S-type, but the S-type can be installed with half the time approximately.

In both designs, the mats have been connected in parallel to the distribution pipes and are tested with two different number of heat exchangers, 16 and 8. In total, four capillary mats combinations have been tested as shown in Table 1.

Two different flat plate heat exchangers have been tested, one made of stainless steel (SS) from the manufacturer Energie Solaire and the other made of polypropylene (PP) from the manufacturer MEFA. The physical

Tab. 1: Heat exchanger data for capillary mats.

Type	n_{hx}	n_{tubes}	L_{tube}	d_i	d_o	A_{hx}	x_{tubes}	x_{hx}
	[-]	[-]	[m]	[mm]	[mm]	[m^2]	[mm]	[mm]
G-16	16	64	1.96	2.75	4.25	30.75	30	30
S-16	16	96	0.98	2.75	4.25	24.06	20	60
G-8	8	64	1.96	2.75	4.25	15.38	30	60
S-8	8	96	0.98	2.75	4.25	12.03	20	120

Tab. 2: Heat exchanger data for flat plates.

Type	n_{hx}	L_{hx}	H_{hx}	A_{hx}	x_{hx}
	[m]	[m]	[-]	[m^2]	[mm]
SS-10	10	1.854	0.834	30.93	100
SS-8	8	1.854	0.834	24.73	125
SS-6	6	1.854	0.834	18.55	167
PP-10	10	1.875	0.860	32.25	100
PP-8	8	1.875	0.860	25.80	125

data of the heat exchangers is given in Table 2.
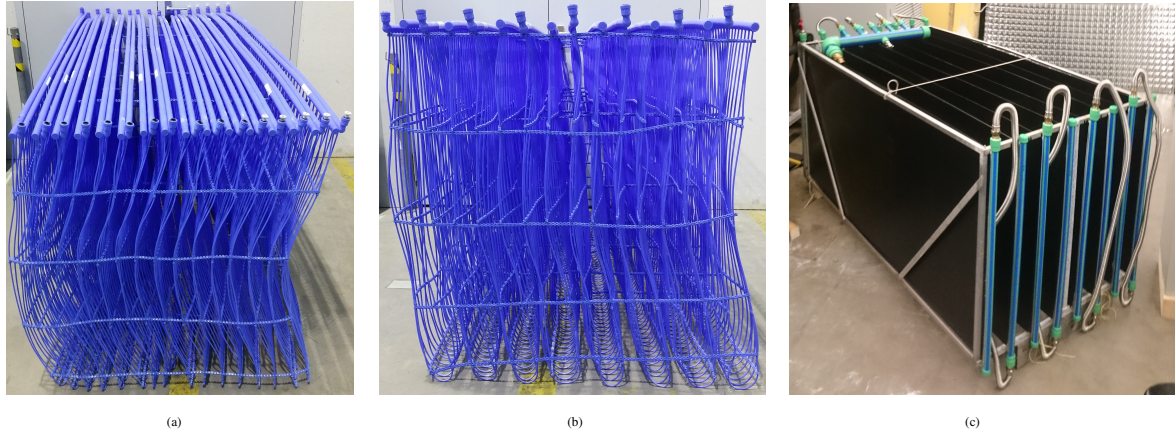
Fig. 2: Examples of heat exchangers (a) 16 S-type capillary mats (b) 8 G-type capillary mats and (c) 8 polypropylene flat plates.

3. Methodology

In order to test the heat exchangers an experimental sequence has been defined and programmed in LabView. The testing sequence is summarized in Table 3. The nominal mass flow rate defined as $\dot{V}_n$ has been set to 2000 l/h. The parameter n is a factor used to reduce the mass flow when desired. All heat exchangers have been tested with n = 1 and with n = 0.5 where the volume flow is regulated with a PID control. Each test lasted around one week for each mass flow and a total of 9 heat exchanger set-ups have been evaluated. This means a total of 18 weeks of testing time are shown in this paper.

3.1. Performance indicators

For each test sequence several indicators are calculated. The heat exchanger power $\dot{Q}$ is calculated as:

$$\dot{Q} = \dot{m}c_p(T_{f,out} - T_{f,in}) \tag{1}$$

Tab. 3: Testing sequences considered for each heat exchanger.

Test phase	Name	Mass Flow	T_{set} of the chiller	Begin of sequence	End of sequence
Sensible heating	T1	$n \cdot \dot{V}_n = 1000$ l/h	20 °C	Storage at 10 °C or end of T8	steady state
	T2	$n \cdot \dot{V}_n = 2000$ l/h	40 °C	End of T1	steady state
Sensible cooling	T3	$n \cdot \dot{V}_n = 1000$ l/h	-10 °C	End of T1	$T_{s,av} \approx 0$ °C
	T4	$n \cdot \dot{V}_n = 2000$ l/h	-10 °C	End of T2	$T_{s,av} \approx 0$ °C
Solidification	T6	$n \cdot \dot{V}_n$ [a]	-10 °C	End of T3 or T4	$V_r \approx 95\%$ (or 3 days)
Cycling : Ice/melt	T8	$n \cdot \dot{V}_n$ [a]	-10 °C (40 min)		
			10 °C (20 min)	End of T6	10 cycles
Melting	T9	$n \cdot \dot{V}_n$ [a]	10 °C	End of T8	steady state

[a] with n=0.5 and n=1

where $\dot{m}$ is the mass flow, c_p the specific heat capacity and T_f the heat transfer fluid temperature. The cumulated energy for the whole test sequence until the time t is calculated as:

$$Q = \int_{t=0}^{t} \dot{Q} \cdot dt \qquad (2)$$

where the time step dt is set to 10 seconds. The ice fraction is calculated as the ratio between the mass of ice and the total amount of water of the storage.

$$V_r = \frac{M_{ice}}{M_{water}} \qquad (3)$$

The ice fraction is experimentally evaluated measuring the change of height of water due to the volume change between water and ice. For some processes, e.g. melting cases where the initial ice fraction is very large and the ice is above water level, the mass of ice can not be accurately obtained from experiments and therefore it is calculated from the energy exchanged with the storage, neglecting heat gains from ambient trough the storage walls. Ice fraction results that are calculated from the exchanged energy are labeled as V_r^*.

The global heat transfer rate of the heat exchanger UA is obtained from:

$$UA = \frac{\dot{Q}}{LMTD} \qquad (4)$$

where the logarithmic mean temperature difference LMTD is calculated as:

$$LMTD = \frac{(T_{f,out} - T_{w,av}) - (T_{f,in} - T_{w,av})}{ln\left(\frac{T_{f,out} - T_{w,av}}{T_{f,in} - T_{w,av}}\right)} \qquad (5)$$

where $T_{w,av}$ is the averaged water temperature in the storage.

The heat transfer coefficient of the heat exchanger is calculated as:

$$U = \frac{UA}{A_{ext}} \qquad (6)$$

where A_{ext} is the external surface area of each heat exchanger

4. Results

The experimental results are split into sensible heating , sensible cooling, icing, melting and cycling of icing/de-icing. Results for flat plates made of polypropylene with a volume flow of 1000 l/h are not shown in the following sections because we have detected problems in the flow distribution.

4.1. Sensible heating (T1 and T2)

Measured overall heat transfer coefficients for sensible heating process with capillary mats and flat plates are shown in Fig. 3 . Circle marks are for 2000 l/h and for T2, i.e. the storage is heated from 20 °C to 40 °C. Filled triangles are for 1000 l/h and for T1, i.e the storage is heated from 10 °C to 20 °C.
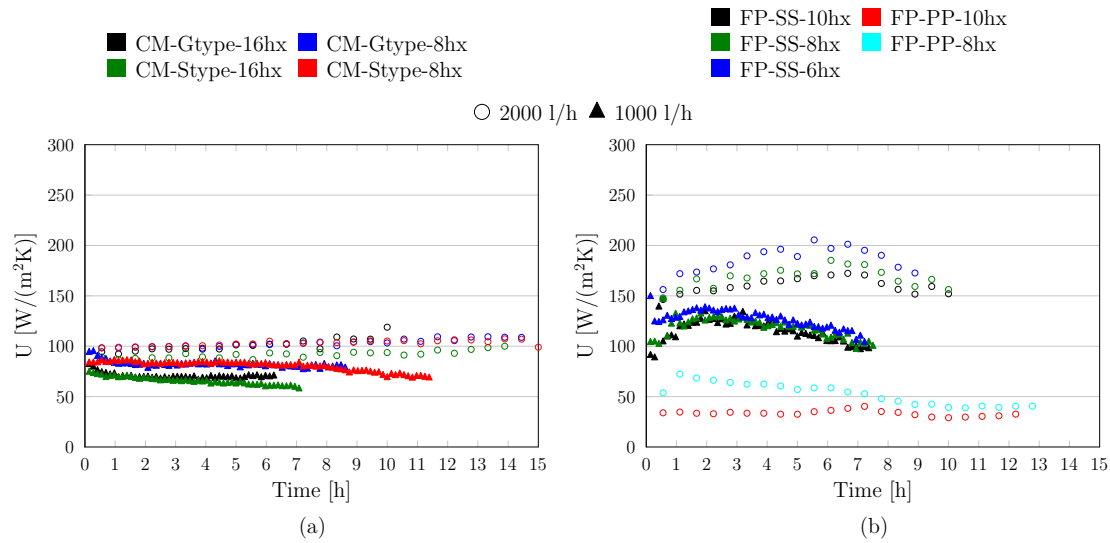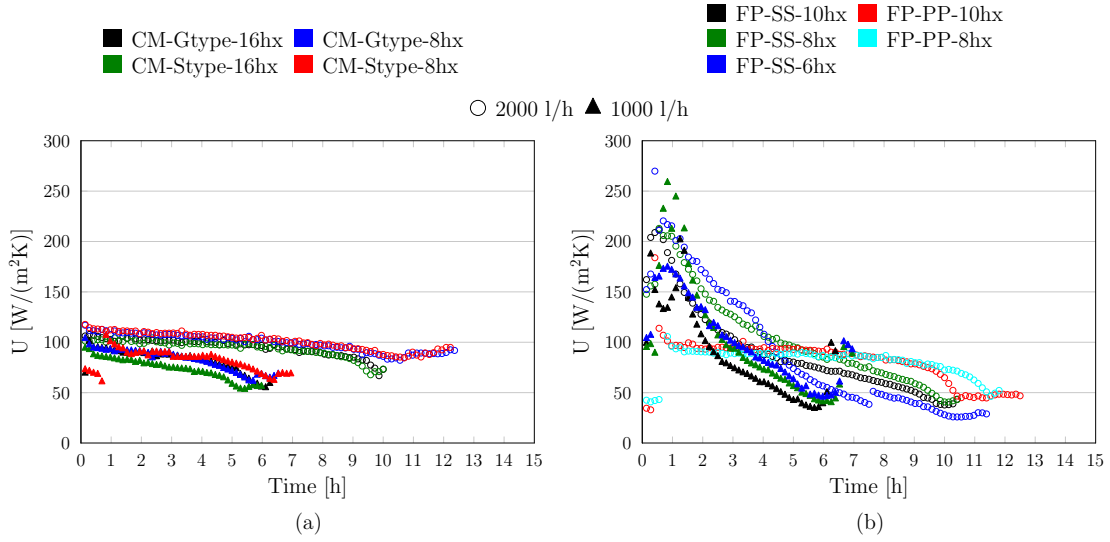

Fig. 3: Overall heat transfer coefficient results for sensible heating sequences T1 and T2 for (a) CM and (b) FP. Circle marks are for 2000 l/h and T2 (heating from 20 °C to 40 °C) and filled triangles are for 1000 l/h and T1 (heating from 10 °C to 20 °C)

The overall heat transfer coefficient U is shown in Fig.3. FP-SS show higher capacities for providing energy to the storage by means of sensible heat. For a flow rate of 2000 l/h, U is in the range of 90-110 W/(m^{2}K) for CM and between 150-200 W/(m^{2}K) for FP with SS. For 1000 l/h U values are decreased to values between 70 and 90 W/(m^{2}K) for CM and to 100-140 W/(m^{2}K) for FP-SS approximately. The main difference between the two different designs of capillary mats, G and S types, is the heat exchanger area as *U* values are very similar. FP-PP show a much lower performance compared to FP-SS and the performance of CM is better than the one of FP-PP but worse than the one of FF-SS. The performance of CM and FP-PP remains relatively constant for all the sequence even that the Reynolds number (Re) increases due to the lower viscosity of the fluid when it is heated. During the whole test sequence the Re number remains below 400 for 2000 l/h and below 150 for 1000 l/h and therefore is always in a theoretical laminar regime. In a laminar flow regime the Nussel number is relatively constant and therefore the performance of the capillary mats are not affected by the increase of Re during the heating process and only slightly due the change of mass flow. However, FP-SS are significantly affected by the mass flow because they have a special design that enhances turbulence. For these type of heat exchangers the Re number where the flow is turbulent is much lower than that for smooth pipes. The flow regime found in these experiments for FP-SS are most of the time in the transition regime between laminar and turbulent and therefore, the Nu numbers, and thus the U values, are affected by the Re number.

4.2. Sensible cooling (T3 and T4)

Overall heat transfer coefficients U for capillary mats and flat plates for sensible cooling process are shown in Fig. 4 . Circle marks represent $\dot{V}_n$ of 2000 l/h and a test sequence in which the storage temperature is cooled from 40 °C to 0 °C. Triangle marks represent $\dot{V}_n$ of 1000 l/h and a test sequence in which the storage temperature is cooled from 20 °C to 0 °C.

The overall heat transfer coefficient shows a very different behavior for CM and FP-SS. For FP-SS, the *U* values decrease significantly with time. For CM the *U* values remain approximately constant for a large time period. The reason for that is the same given in section 4.1, i.e. capillary mats are always in a laminar regime while

Fig. 4: Overall heat transfer coefficient results for sensible cooling sequences T4 for (a) CM and (b) FP. Solid lines are for 2000 l/h and the cycle starts at T_s of 40 °C; dashed lines are for 1000 l/h and the cycle starts at T_s 20 °C

FP-SS are in the turbulent and transition regime. In this case, the Re number decreases along the sequence because the fluid's viscosity is increased when cooled down to 0 °C. At the beginning of the test sequence, FPs perform significantly better than the CMs, and the opposite is true at the end of the test sequence. The U values range from 120 to 75 W/(m²K) for 2000 l/h and from 100 to 60 W/(m²K) for 1000 l/h when CMs are used; and they range from 220 W/(m²K) to 40 W/(m²K) using 2000 l/h and from 175 W/(m²K) to 40 using 1000 l/h when FP-SS are used. The evolution of U along time for FP-PP is similar to the one observed with CM when 2000 l/h are used. The U values are relatively constant and in the range of 100 W/(m²K) for a large period. The efficiency of the heat exchangers is reduced when the storage water temperature is close to 0 °C, when ice starts to grow, the U value increases.

4.3. Solidification (T5)

The amount of ice produced for capillary mats and for flat plates are shown in Fig. 5. From these results it seems clear that capillary mats are faster compared to flat plates in the process of water solidification. Ice fractions above 95 % were achieved with CM without damaging the casing. Due to the specific height of the
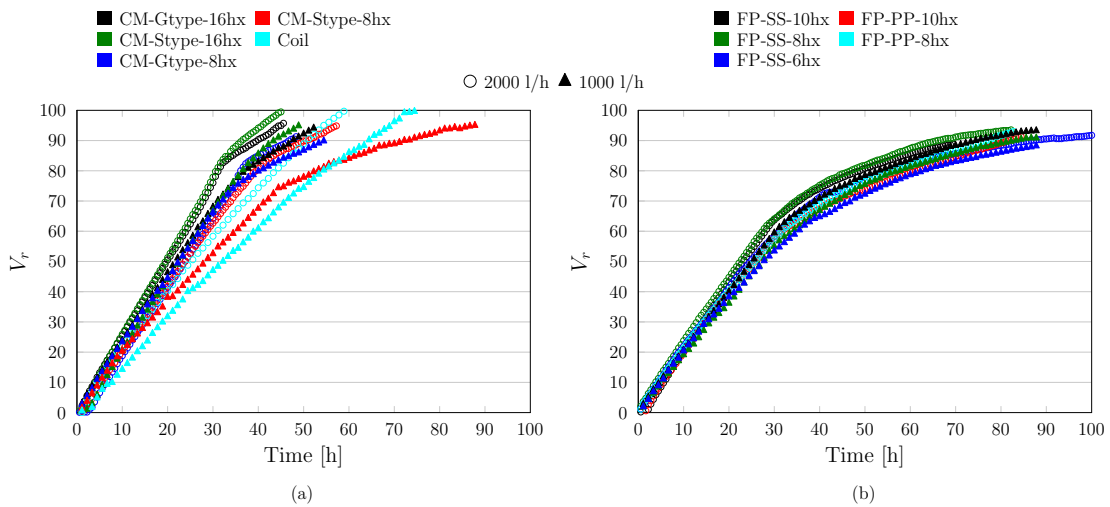
Fig. 5: Evolution of the ice fraction over time for the icing sequence T5 for (a) CM and (b) FP.

FP, only 85% of the storage height was covered by the heat exchangers, limiting its capacity to ice the whole storage. Mass ice fractions higher than 85% with FP are possible but with very low power since ice has to grow on the surface of a compact ice cube that includes all plates with a long path between the heat transfer fluid in the heat exchanger and liquid storage water. For FP, ice fractions above 90% where achieved and the casing of the storage did not show any problem.
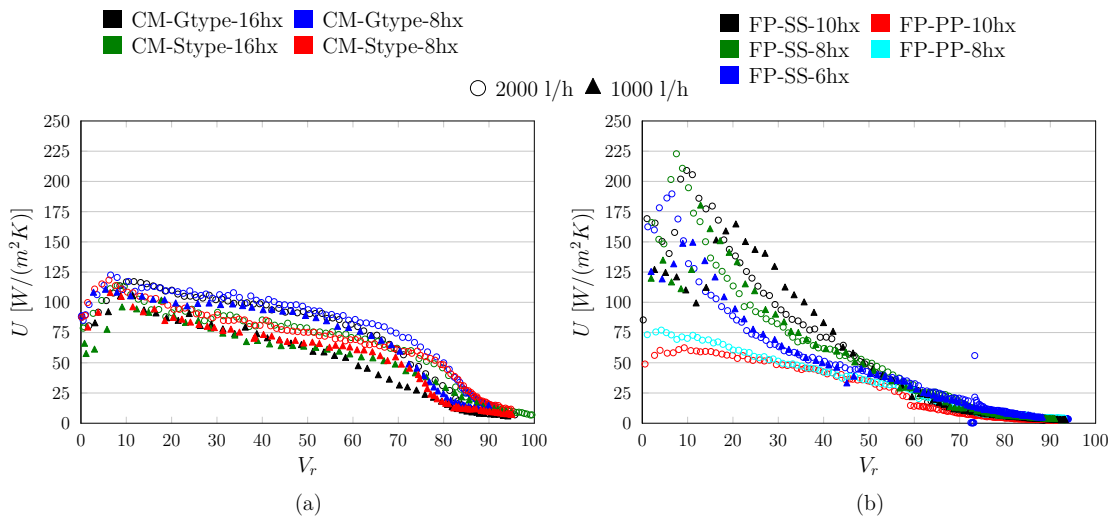

Fig. 6: Overall heat transfer coefficient as a function of the ice fraction for the icing sequence T5 for (a) CM and (b) FP.

The overall heat transfer coefficient is shown in Fig. 6 as a function of the ice fraction. From this graph it can be observed that the decrease of U for CM is much smaller compared to FP. Considering the ideal case of ice growing on a single tube, the higher thermal resistivity of the ice layer when ice grows is partially compensated by the higher contact area on the outside of the tube. Therefore, the heat transfer rate UA value remains relatively constant when ice grows on a cylinder (Carbonell et al., 2015). However, CM, are composed of many tubes very close to each other and the ideal unidimensional ice growing on a single tube is only valid until ice growing from neighboring tubes contact with each other. For example, for the S-type, the distance between tubes in one heat exchanger is 20 mm. Assuming that ice grows homogeneously on all pipes and along the whole pipe length, ice layers start to touch to each other within one heat exchanger when V_r is approximately 27% and 14% for 16 hx and 8 hx respectively. For G-type, the distance between pipes is 30 mm, this means that ice layers between pipes touch when the ice fraction is approximately 80% and 40% for 16 hx and 8 hx, respectively. The phenomenon of physical contact between ice layers is usually called constrained ice growing (Jekel et al., 1993). For all CM, the heat exchangers suffer of a two step constrained ice growing, the first one when the ice is constrained within one heat exchanger (ice between adjacent tubes touch each other) and the second when ice is constrained between neighboring heat exchangers. When ice growing is constrained the overall heat transfer coefficient decreases compared to the unconstrained case because the contact area between the growing ice and storage water decreases. However, in the experimental results it is not possible to observe a sharp decrease of the U value when ice constrainment occurs because ice grows unequally along the length of each tube and thus the ice growing is constrained slowly over a long period. For FP ice starts to be constrained when the ice thickness is half the distance between heat exchangers. This corresponds always to an ice fraction of approximately 83%. At these conditions all water between heat exchangers is frozen and ice can only grown on the surface of a solid cube of ice with very low U values. Comparing CM with FP one can observe that for low ice fractions the U values of FP-SS are higher. However, the decrease of the U value when ice grows is much more pronounced for FP-SS compared to CM. As said before, the contact area between ice and water increases when ice grows in CMs. Instead, for FPs the ice surface area remains approximately constant and the U value decreases rapidly. For FP with PP, the decrease of efficiency is much less pronounced in comparison to SS because the heat transfer resistance of the polypropylene is the limiting factor, in comparison to the FP-SS

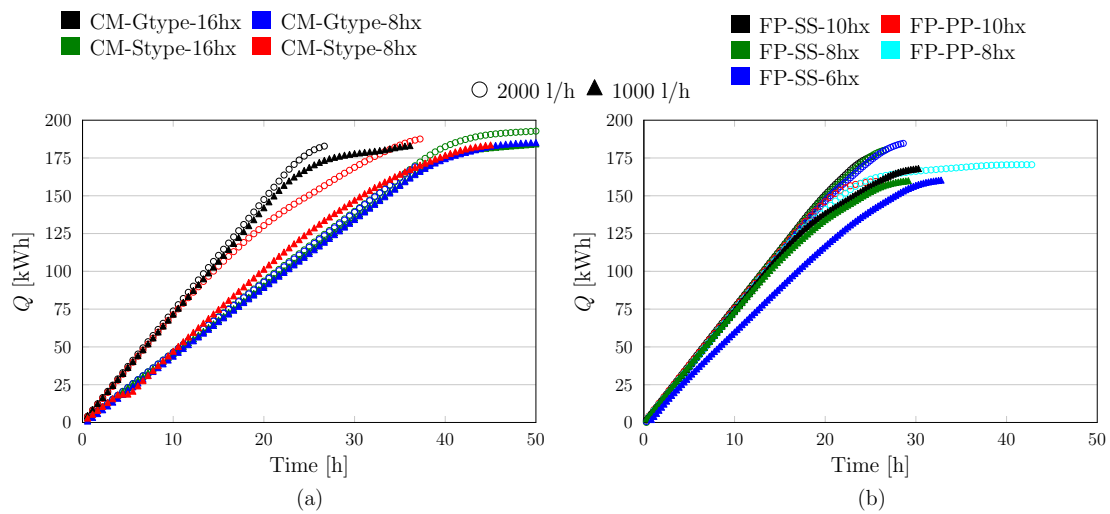where the ice thickness is the limiting factor.

4.4. Melting (T9)

Fig. 7: Energy delivered to the storage by the heat exchangers for the melting sequence T9 for (a) CM and (b) FP.

The energy delivered for melting the ice is shown in Fig. 7. Melting 2 m^3 of water needs about 185 kWh. On top of that, the energy needed to heat the subcooled ice to 0 ^{o}C and the sensible heat to raise the temperature from 0 ^{o}C to 10 ^{o}C needs to be considered. Comparing CM with FP one can observe that FP-SS are usually able to melt completely the ice in less time. The measure for the ice fraction for capillary mats was not accurate with the method used in these experiments. A water layer above the ice block was not always present at high ice fraction (> 95%) and the measure of solid ice was disturbing the accuracy. Because the flat plates had a layer of 17 cm of water above them, the measurement of the melted ice were much more accurate. However, even in this case, with the method used, it is not possible to measure the ice fraction until the melted ice connects to the water of the storage. Before this cavity of ice is melted, the change of density when the ice is melted creates an underpressure around the hx that would either expand the heat exchanger or evaporate part of the water until the change of volume is filled.

Overall heat transfer coefficients are shown in Fig. 8. FP-SS have the highest melting capacity at high ice fractions with values above 250 W/(m^{2}K). For ice fractions below 60% the U values reduce to 50-60 W/(m^{2}K) for FP with SS. For CM, the U values are more stable over the whole melting process with values between 50-80 W/(m^{2}K).

4.5. Cycling (T8)

The cycling experiment consist of 10 sequences of heating and cooling which are used for melting and icing. This test sequence is performed at a very high ice fraction after the icing sequence T5. Each cycle is performed with a constant time of 20 min for heating and 40 min for cooling. All experiments with CM were tested with cycles always on the subcooled zone and therefore melting was not achieved. For this reason the test control was changed such that it heats up the storage until the outlet of the heat exchanger is close to zero before cycling starts. In this way it is ensured that ice is melted and solidified during each cycle. As an example, results for cycling sequence are presented in Fig. 9 for FP with 10 hx. For all the cycles the inlet temperature of the heat exchangers increases above 0 ^{o}C, which means that it is always possible to melt ice, at least the entrance of the heat exchangers. For the first four cycles, the outlet temperature remains at 0 ^{o}C, which means
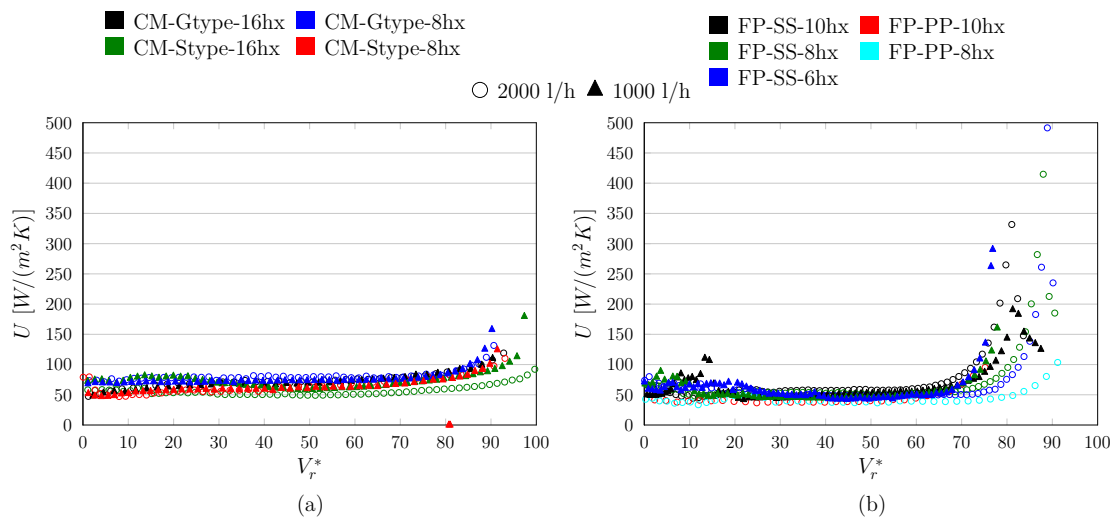
Fig. 8: Overall heat transfer coefficient for melting sequence T9 for (left) CM and (right) FPs.

that ice is never subcooled at the end of the heat exchanger. After the first cycles, the outlet temperature starts to drop below 0 °C which means that ice is subcooled, and the UA values are reduced because the heat of fusion is not released along the whole length of the hx.
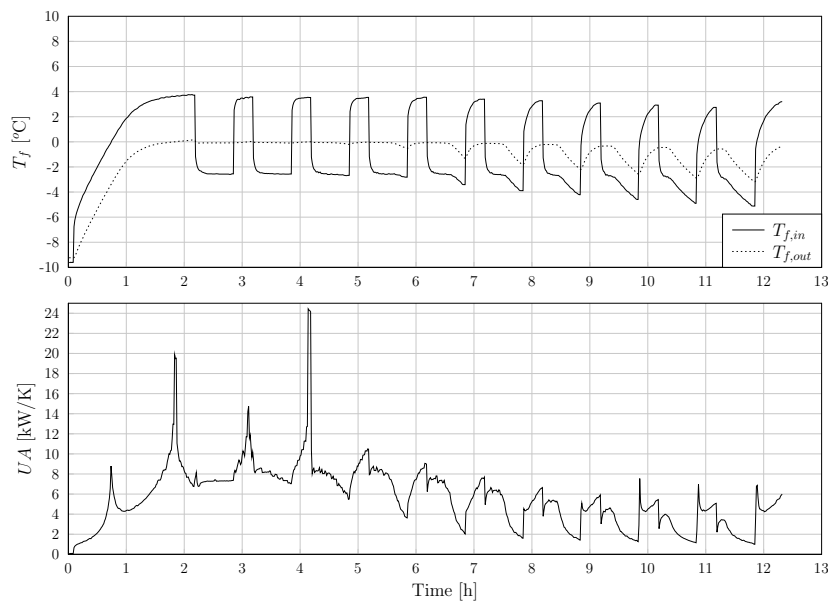

Fig. 9: (a) Heat exchanger temperatures and (b) overall heat transfer coefficient for cycling sequence T8 and FP.

The danger of breaking the casing of the storage is potentially higher when cycles of melting and icing exist at high ice fractions. In normal icing conditions without any cycles, the solid ice will always push the liquid water to the surface. Therefore, as long as there is an escape way for the water, there is no risk for the casing. The problem may occur when a volume of water in contact with the casing is trapped within an ice block. If then this water is iced, the volume expansion will produce a strong force to the wall of the casing with the danger of breaking it. This situation may occur when the dynamics of the system are on a specific state, which was never the case in the lab.

In this test several cycles of melting and icing have been performed at very high ice fractions in order to test the robustness of the heat exchangers under these dynamic conditions. The mechanical stress that was caused

by the dynamics of icing and melting was neither found to be a problem for the heat exchangers nor for the storage casing. However, long term tests should be performed to investigate the robustness and stability.

The cycling sequence will also be very useful for the validation of the ice storage model (not provided in this paper), since in each cycle different physical phenomena take place. Fig. 10 shows one cycle of melting and icing for FP-SS with 10 hx (zoom into Fig. 9). The sequence has been split into five zones, from I to V as shown in Fig. 10. Zones I to II correspond to heating/melting and zones III to V correspond to cooling/icing.

- Zone I : switch from cooling to heating.

- Zone II: the ice is heated from the subcooled state to 0 °C and melted starting from the entrance of the heat exchangers. Most likely, melting does not occur over the whole length since the outlet temperature remains below 0 °C.

- Zone III: cooling of the water until freezing conditions.

- Zone IV: icing of the water.
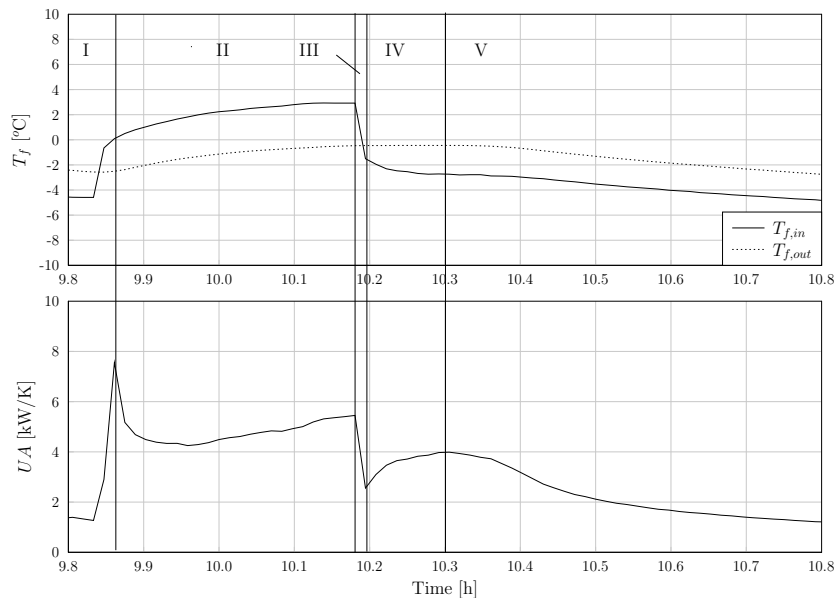
- Zone V: subcooling of ice.

Fig. 10: (a) Heat exchanger temperatures and (b) heat transfer rate for cycling sequence T8 and FP.

5.   Conclusions and future actions

In the present work several heat exchangers have been analyzed, including capillary mats with different designs made of polypropylene and flat plates made of stainless steel and polypropylene. The area analyzed has been modified for each heat exchanger and all test have been performed using two different mass flow rates. In total, nine possibilities have been experimentally evaluated for several test sequences including sensible heating and cooling, icing, melting and cycling. The main conclusions of the study can be summarized as:

- Very high ice fraction can be reached with all heat exchangers and mass flows.

- The casing did not show any damage under high ice fraction conditions. This means that designing an ice storages able to reach 95% ice fraction or higher should be safe.

- All heat exchangers showed to be reliable and robust under the test conditions. Long term tests were not carried out.

- Flat plates made of stainless steel are better suited compared to capillary mats for sensible heating and cooling and for melting processes.

- Capillary mats are better suited compared to flat plates for the icing process due to the strong decrease of performance that flat plates suffer when ice grows.

- Flat plates made of polypropylene have shown the worst thermal performance of all tested hxs.

- The poor flow distribution for 1000 l/h in the case of flat plates made of polypropylene needs to be further investigated.

An ice storage model able to consider all these heat exchanger designs has been developed and it is being validated with the experiments presented here. As a next step, system simulations with TRNSYS will be carried out with the validated ice storage model. With these simulations, it will be possible to find an optimum between the energetic system efficiency and the cost of the ice storage as a function of the heat exchanger area.

Acknowledgments

References

ASHRAE, 2007. Handbook : HVAC Applications. American Society of Heating, Refrigerating and Air-Conditioning Engineers, Inc.

Carbonell, D., Philippen, D., Granzotto, M., Haller, M.Y., 2016a. Simulation of a solar-ice system for heating applications. system validation with one-year of monitoring data. Energy and Buildings 127, 846 – 858.

Carbonell, D., Philippen, D., Haller, M.Y., 2016b. Modeling of an ice storage buried in the ground for solar heating applications. Validations with one year of monitored data from a pilot plant. Solar Energy 125, 398–414.

Carbonell, D., Philippen, D., Haller, M.Y., Frank, E., 2015. Modeling of an ice storage based on a de-icing concept for solar heating applications. Solar Energy 121, 2–16.

Jekel, T.B., Mitchell, J.W., Klein, S.A., 1993. Modeling of ice storage tanks. ASHRAE Transactions 99, 1016–1024.

Philippen, D., Haller, M.Y., Logie, W., Thalmann, M., Brunold, S., Frank, E., 2012. Development of a heat exchanger that can be de-iced for the use in ice stores in solar thermal heat pump systems, in: Proceedings of EuroSun, International Solar Energy Society (ISES), Rijeka and Opatija, Croatia.

Tamasauskas, J., Poirier, M., Zmeureanu, R., Sunyé, R., 2012. Modeling and optimization for a solar assisted heat pump using ice slurry as a latent storage material. Solar Energy 86, 3316–3325.

Trinkl, C., Zörner, W., Hanby, V., 2009. Simulation study on a domestic Solar/Heat pump heating system incorporating latent and stratified thermal storage. Journal of Solar Energy Engineering 131, 041008.

Winteler, C., Dott, R., Afjei, T., Hafner, B., 2014. Seasonal performance of a combined solar, heat pump and latent heat storage system. Energy Procedia 48, 689–700. Proceedings of the 2nd International Conference on Solar Heating and Cooling for Buildings and Industry (SHC 2013).